FISEVIER

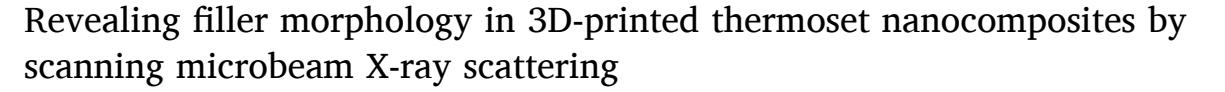
Contents lists available at ScienceDirect

# Additive Manufacturing

journal homepage: www.elsevier.com/locate/addma



# Research Paper



Edward B. Trigg <sup>a,1</sup>, Nadim S. Hmeidat <sup>b,2</sup>, Louisa M. Smieska <sup>c,3</sup>, Arthur R. Woll <sup>c,4</sup>, Brett G. Compton <sup>b,d,5</sup>, Hilmar Koerner <sup>a,\*,6</sup>

- <sup>a</sup> Materials & Manufacturing Directorate, Air Force Research Laboratory, WPAFB, OH 45433, United States
- <sup>b</sup> Mechanical, Aerospace, and Biomedical Engineering Department, University of Tennessee, Knoxville, TN 37996, United States
- Cornell High Energy Synchrotron Source, Cornell University, Ithaca, NY 14850, United States
- <sup>d</sup> Materials Science and Engineering Department, University of Tennessee, Knoxville, TN 37996, United States

#### ARTICLE INFO

# Keywords: Direct ink write Epoxy Composite Scanning microbeam X-ray scattering

#### ABSTRACT

Room temperature direct-ink-write printing of epoxy-nanoclay-carbon fiber composites produces parts with high stiffness and strength. Establishing clear relationships between print parameters, filler orientation, and properties is difficult, in part owing to challenges in characterization. Here, we perform scanning microbeam X-ray scattering with 5 micrometer spatial resolution on cross-sections of printed parts with (a) epoxy-nanoclay composite and (b) epoxy-nanoclay-carbon fiber reinforced composite. The nanoclay morphology is directly visualized, illuminating the road geometry with far greater clarity than other techniques. Near the boundary of each road, the nanoclay platelets are preferentially oriented coplanar with the road boundary. Shear alignment within the nozzle during extrusion, and road-to-road shear upon deposition are two proposed factors leading to this orientation. In the sample containing carbon fiber, wide angle X-ray diffraction enables the mapping and visualization of the fibers directly onto the road geometry. The carbon fiber does not significantly affect the nanoclay morphology. Finally, from the small angle X-ray scattering map, we qualitatively reproduce a polarized optical microscope image, revealing that optical microscopy is capable of visualizing the large-scale road structure in these epoxy-nanoclay systems.

# 1. Introduction

Among the many promising capabilities of additive manufacturing is the ability to tailor the morphology and microstructure of the printed material with spatial specificity within each road that is laid down onto the build plate. Not only can the printed parts have complex, previously unmanufacturable shapes, but they can also have material properties that vary within the part – for example, dictated by differences in alignment or degree of crystallinity [1-6]. As such, there is a need for techniques that can provide spatially-resolved characterization of the morphology of printed parts to be able to control this additional degree

of freedom.

Additive manufacturing of thermoset composites is of particular interest to the aerospace industry due to the potential for agile manufacturing of high-performance complex parts [7]. Room temperature direct ink write (DIW) printing of epoxy-carbon fiber composites has been developed recently, enabled by the addition of either fumed silica [8,9] or nanoclay [1,10,11], which are rheology modifiers that provide a high yield stress so the material retains its shape after deposition onto the build plate. If nanoclay is used, the extrusion process aligns the nanoclay, significantly influencing mechanical properties of the final part after cure [12]. This recent study, by Hmeidat et al.,

E-mail address: hilmar.koerner.1@us.af.mil (H. Koerner).

- $^{1}$  ORCID Id 0000-0002-4723-650X
- <sup>2</sup> ORCID Id 0000-0002-9669-0426
- <sup>3</sup> ORCID Id 0000-0001-8150-1920
- $^4$  ORCID Id 0000-0001-8925-2199
- <sup>5</sup> ORCID Id 0000-0001-5480-474X
- <sup>6</sup> ORCID Id 0000-0002-1864-8193

https://doi.org/10.1016/j.addma.2020.101729

<sup>\*</sup> Corresponding author.

measured a direct relationship between average Hermans orientation factor for the nanoclay, the strength and stiffness of the printed composite, and the diameter of the deposition nozzle used to print the test specimen. In addition, cross-polarized light microscopy showed that periodic birefringence patterns in the printed specimens closely correspond to the size and location of individual printed roads, suggesting a unique spatial arrangement of the nanoclay within printed composites. However, despite these and other studies that have utilized SEM and optical microscopy, the location-dependent orientation of the nanoclay in printed polymer/nanoclay composites is poorly understood [1,10,13, 14].

Scanning microbeam small- and wide-angle X-ray scattering (µ-SAXS/WAXS) is a powerful synchrotron technique that probes the morphology of an array of micrometer-size regions in a sample [15–17]. High resolution 2D SAXS and WAXS patterns are recorded for every such region in a grid across the scan area, and maps are generated with resolution similar to optical microscopy (1–10  $\mu m$ ). These data provide information at the nanoscopic scale, including crystalline structure and orientation within each 1-10 µm pixel of the resulting map. Such information is complementary to that obtained by X-ray computed tomography (CT), another X-ray based technique that is frequently used to assess filler morphology in composites. Compared to u-SAXS/WAXS, X-ray CT has the advantage of providing 3D information at a comparable or even superior length scale, but generally provides only the average relative electron density of each pixel/voxel. For the samples described here more specifically, X-ray CT cannot probe the nanoclay orientation. High-resolution CT also imposes more stringent requirements on the sample dimensions, while μ-SAXS/WAXS only requires a sample thickness suitable for scattering experiments (typically 0.1-2 mm). The combination of CT and scanning microbeam techniques thus provide access to length scales from the nanometer to millimeter scale [18].

In this work, we use  $\mu$ -SAXS/WAXS to characterize 3D-printed epoxy-based samples. We directly visualize the road structure (inaccessible by methods such as SEM and X-ray CT), quantify the morphology of the nanoclay, and map the carbon fiber locations. In doing so, we demonstrate the utility of this scanning technique for spatially resolved morphological characterization of any 3D-printed material.

#### 2. Methods

# 2.1. Materials

The thermoset resin used was EPON 826 (Hexion, Inc., Columbus, OH), a Bisphenol A diglycidyl ether (DGEBPA) resin with 178-186 wt per epoxide, and density of 1.16 g/cm<sup>3</sup>. Amicure CG-1200G (Evonik Industries AG, Essen, Germany), a dicyandiamide (DICY) powder, was employed as a latent curing agent for the epoxy resin. GARAMITE 7305 nanoclay (NC) (BYK-Chemie GmbH, Wesel, Germany), a blend of benzalkonium sepiolite and benzalkonium montmorillonite, with a density of 1.6 g/cm<sup>3</sup>, was utilized as a nanoscale filler material and viscosity modifier, following Hmeidat et al [10]. The sepiolite is a micro-fibrous magnesium phyllosilicate with length of 2-10 µm [19], and a specific surface area up to 200–300  $\mbox{m}^2/\mbox{g},$  which implies an average diameter of 10-100 nm [20]. The montmorillonite is a layered silicate with a thickness of ~1 nm and a lateral dimension of ~100 nm in the fully dispersed state [21,22]. K223HM milled carbon fibers (CF) (Mitsubishi Chemical Carbon Fiber and Composites, Inc., Tokyo, Japan) were utilized as microscale reinforcement filler materials. K223HM CFs are unsized, pitch-based fibers with 11  $\mu m$  diameter, 200  $\mu m$  mean length, and density of 2.2 g/cm<sup>3</sup>.

# 2.2. DIW ink formulation

Two DIW inks were formulated using a centrifugal planetary mixer (FlackTek, Inc., Landrum, SC). Inks were prepared by initially mixing 20

g of epoxy resin with 1 g of the curing agent at 1700 rpm for 1 min. Next, 2.33 g of NC was added, followed by 1 min of mixing at 1800 rpm. Finally, the formulation was mixed for an additional 2 min at 2000 rpm. This formulation is referred to as the NC ink. The second formulation, referred to as the NC/CF ink, was made by adding 0.3 g CF after the first mixing step with the NC filler, followed by mixing at 2000 rpm for 2 min. All mixing steps were performed under vacuum at 100 mbar to eliminate void formation and trapped air pockets. Ink formulations are summarized in Table 1.

# 2.3. 3D-printing and curing protocol

Inks were printed using a 3-axis positioning stage (ShopBot Tools, Inc., Durham, North Carolina), equipped with a pneumatic extrusion system. Inks were loaded into 10 cc syringes (Nordson EFD, Westlake, OH) and centrifuged at 3900 rpm for 8 min using a Sorvall<sup>TM</sup> ST-8 Centrifuge (ThermoFisher Scientific, Waltham, MA), to remove any trapped air pockets that arise during the loading process, following Refs. [10,1]. The deposition nozzle was a tapered metal nozzle tip (S-type, GPD, Grand Junction, CO) with an inner diameter (ID) of 609 um. The layer height was set to 0.6 times the ID of the nozzle (365 um), and the lateral road spacing was set to 0.85 times the ID (518 um) [10]. A constant translation speed of 20 mm/s was used for all prints. An extrusion pressure of 50 psi was used for both inks and resulted in a flow rate matched to the translation speed of the print head. Rectangular specimens with nominal dimensions of 40 mm  $\times$  8 mm  $\times$  2 mm were printed on a glass substrate covered with polytetrafluoroethylene (PTFE) coated aluminum foil (Bytac, Saint-Gobain Performance Plastics, Worcester, MA) to prevent permanent adhesion. Printed samples were then cured at 120  $^{\circ}$ C for 24 h.

#### 2.4. Scanning microbeam SAXS/WAXS

Thin (0.4 mm) slices of the two printed rectangular samples were cut orthogonal to the printing direction for the X-ray experiments. Samples were cut using a low speed sectioning saw (TechCut 4, Allied High Tech Products, Inc., Rancho Dominguez, CA). Surfaces of the cut slices were then polished using aluminum oxide lapping films (Allied High Tech Products, Inc.), where the finest particle size used was 3  $\mu m$ . X-ray scattering was performed at the Functional Materials Beamline (FMB, ID-3B) of the Materials Solution Network (MSN-C) at the Cornell High Energy Synchrotron Source (CHESS). The X-ray energy was 9.737 +/-0.0015 keV, selected using a diamond (111) side-bounce monochromator [23] in Bragg geometry. Harmonic rejection was provided by a rhodium-coated vertical-bounce, bendable mirror just downstream of the monochromator. Berylium compound refractive lenses (RXOptics GmbH & Co) were employed just upstream of the sample to create a 2.5  $\mu m$  tall  $\times$  10  $\mu m$  wide X-ray beam, with an approximate intensity of  $10^{10}$ photons/second in the focal spot. SAXS was collected by a Pilatus 200 K detector 0.985 m from the sample. Simultaneously, WAXS was collected by a Pilatus 100 K detector 0.14 m from the sample. Scans were performed in "flyscan" mode, in which the sample is translated continuously in the vertical direction, and the detectors are triggered at each 5 μm (or 0.1 s) interval. Each vertical sweep of the sample is followed by a horizontal translation and vertical carriage return, at which time the next sweep begins. Each complete 2D map took approximately 3.5 h to complete, and comprises 225,060 scattering patterns. The SAXS data were calibrated with silver behenate using the Datasqueeze software [24], and the WAXS data were calibrated with lanthanum hexaboride using the pyFAI package [25].

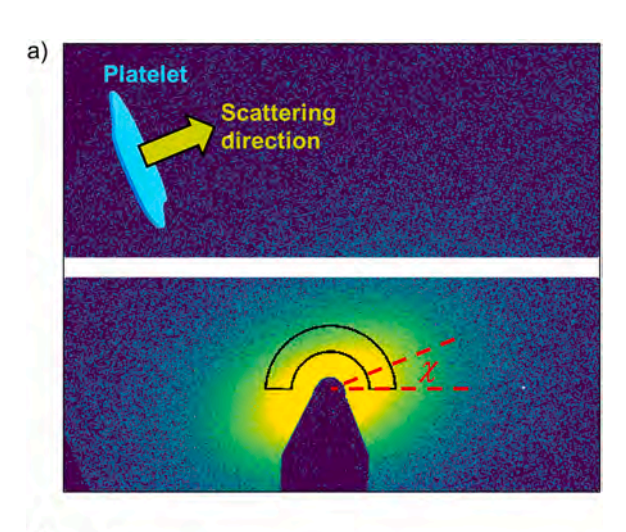
# 2.5. Analysis of SAXS patterns

For each SAXS pattern, the azimuthal intensity distribution was obtained in the q range 0.03–0.05 Å $^{-1}$  (see Figs. 1 and S1) using a custom Python code. This q range was selected to maximize signal while

**Table 1**Ink formulations.

Ink name	Epoxy (g)	Amicure (g)	NC (g)	NC (wt%)	CF (g)	CF (wt%)	CF (vol%)	Density (g/cm <sup>3</sup> ) <sup>a</sup>
NC	20	1	2.33	10	0	0	0	1.22
NC/CF	20	1	2.33	10	0.3	1.27	0.7	1.23

<sup>&</sup>lt;sup>a</sup> Based on a value of 1.183 g/cm<sup>3</sup> for the cured epoxy [11] and 1.90 g/cm<sup>3</sup> for the carbon fiber.



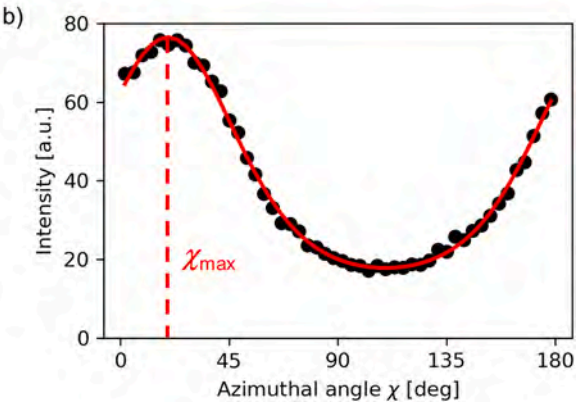


**Fig. 1.** (a) Representative 2D SAXS pattern from the NC sample. The scattering is anisotropic due to nanoclay orientation. The illustration shows the primary direction of scattering, where the incident beam is into the page. (b) Azimuthal intensity distribution from (a) in the q range 0.03–0.05 Å $^{-1}$  is plotted as black circles. The fit to Eq. (1) is shown in red. The black outline in (a) indicates the region of integration to obtain the plot in (b). The intensity in (a) is shown on a logarithmic scale.

minimizing parasitic scattering at low q. The intensity as a function of azimuthal angle  $\chi$  was fit with a Maier-Saupe function: [26,27].

$$I(\chi) = Ac \quad \exp\left[p\cos^2(\chi - \chi_{max})\right] + I_0 \tag{1}$$

where the normalization constant c is given by

$$c = 2p^{1/2} \left[ \pi^{1/2} \operatorname{erfi}(p^{1/2}) \right]^{-1}$$
 (2)

The fitting parameters are A, the amplitude; p, which describes the breadth of the orientation distribution;  $\chi_{max}$ , the angle of maximum scattering; and  $I_0$ , an intensity offset term.

The extent of orientation f for each SAXS pattern was calculated using a modified Hermans orientation function:

$$f = \frac{3}{2} \left\langle \cos^2(\chi - \chi_{max}) \right\rangle - \frac{1}{2}$$

$$= \frac{3}{2} \frac{\int_0^{\frac{\pi}{2}} I(\chi - \chi_{max}) \sin(\chi - \chi_{max}) \cos^2(\chi - \chi_{max}) d(\chi - \chi_{max})}{\int_0^{\frac{\pi}{2}} I(\chi - \chi_{max}) \sin(\chi - \chi_{max}) d(\chi - \chi_{max})} - \frac{1}{2}$$
(3)

where  $\chi_{max}$  is obtained from the Maier-Saupe fit and is therefore different for each SAXS pattern.  $I(\chi)$  is the SAXS intensity, integrated from q= 0.03–0.05 Å<sup>-1</sup>, at azimuthal angle  $\chi$ . The extent of orientation f is not the Hermans orientation parameter, because the type of orientation is not necessarily uniaxial [28,29]. Like the Hermans, when f=0, the azimuthal intensity distribution is isotropic, and when f=1,  $I(\chi)$  is a delta function centered at  $\chi_{max}$ .

# 2.6. Analysis of WAXS patterns

The WAXS data was reduced to I vs. q curves using pyFAI [25]. Mapping of the carbon fibers (Fig. 5d) was accomplished by taking the ratio of the intensity at  $q=1.77~\text{Å}^{-1}\pm0.05$  (graphitic diffraction) to the intensity at  $q=2.24~\text{Å}^{-1}\pm0.05$  (region with no peaks). The intensity value of each pixel in the map was set to this ratio. To map the nanoclay (Fig. 6), peaks at 1.380, 1.465, 2.160, and 2.385  $\text{Å}^{-1}$  were integrated, and the sum of these integrations normalized to the intensity at 2.24  $\text{Å}^{-1}$  was used as the pixel intensity in the map. Further detailed analysis of the WAXS pattern is complicated by the nature of the mixture of fibrils and platelets and is beyond the scope of this paper.

The carbon fiber extent of orientation was calculated using a simplified model. From the binary carbon fiber map shown in black in Fig. 5e, each carbon fiber's area and Feret length was calculated using the ImageJ software [30]. Carbon fibers with area smaller than 5 pixels were excluded, and the Feret lengths were taken as the apparent carbon fiber lengths. The distribution of apparent lengths was modeled by assuming that the apparent length of a carbon fiber is given by

$$\ell = d + L\sin\varphi \tag{4}$$

where d is the average fiber diameter, L is the average fiber length, and  $\varphi$  is the angle between the carbon fiber's axis and the printing direction. Assuming  $\varphi$  is normally distributed about the printing direction, and solving for  $\varphi$  in Eq. 4, the probability density function for apparent lengths is

$$P(\ell) = A \quad \exp\left[-\frac{1}{2}\left(\frac{\varphi(\ell)}{\sigma}\right)^{2}\right] = A \quad \exp\left[-\frac{1}{2}\left(\frac{\sin^{-1}\ell - d}{\sigma}\right)^{2}\right] \tag{5}$$

where  $\sigma$  is the standard deviation of  $\varphi.$  The fit in Fig. 5f uses Eq. 5. From the mixing and section procedures, a conservative (low-end) estimate of the average fiber length is  $100~\mu m$  (reduced from the manufacturer's reported length of  $200~\mu m).$ 

# 2.7. Optical microscopy

Cross-polarized optical microscopy was performed in transmission on a VHX-5000 digital microscope (Keyence Corporation of America, Itasca, IL). The same samples from the X-ray experiments were used, but the regions of the samples were not the same.

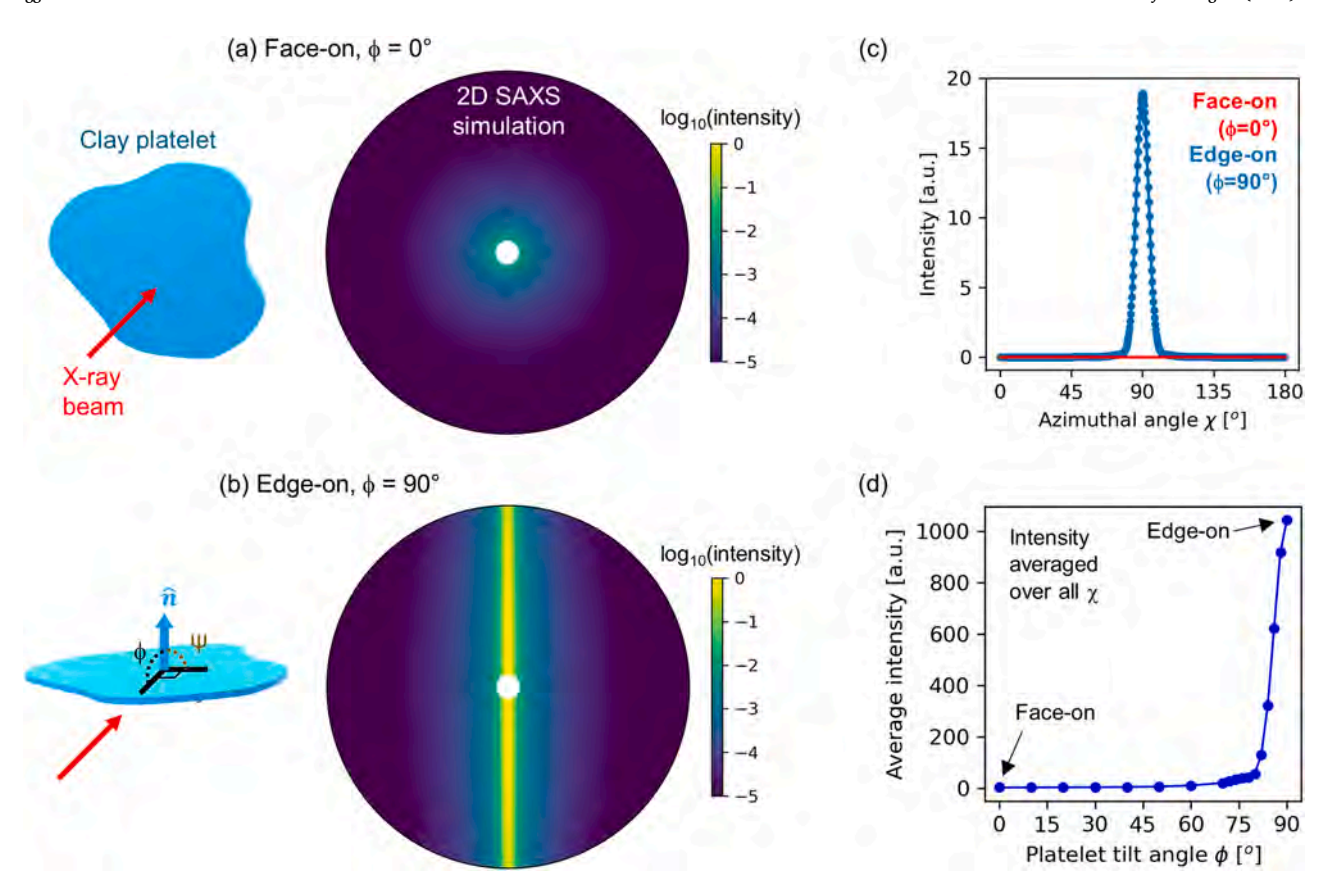


**Fig. 2.** Simulations of SAXS form factor patterns from nanoplatelets at various orientations relative to the incident beam, based on equations presented by Bihannic et al [28]. (a) 2D SAXS pattern simulation for a clay platelet oriented face-on, as shown in the illustration. The incident X-ray beam is into the page. (b) 2D SAXS pattern simulation for a edge-on platelet. (c) Scattering intensity vs. azimuthal angle  $\chi$  for (a) and (b), in the q range 0.03–0.05 Å<sup>-1</sup>.  $\chi$  = 0 is defined as the horizontal direction. (d) Intensity, averaged over all  $\chi$  and in the q range 0.03–0.05 Å<sup>-1</sup>, as a function of platelet tilt angle.

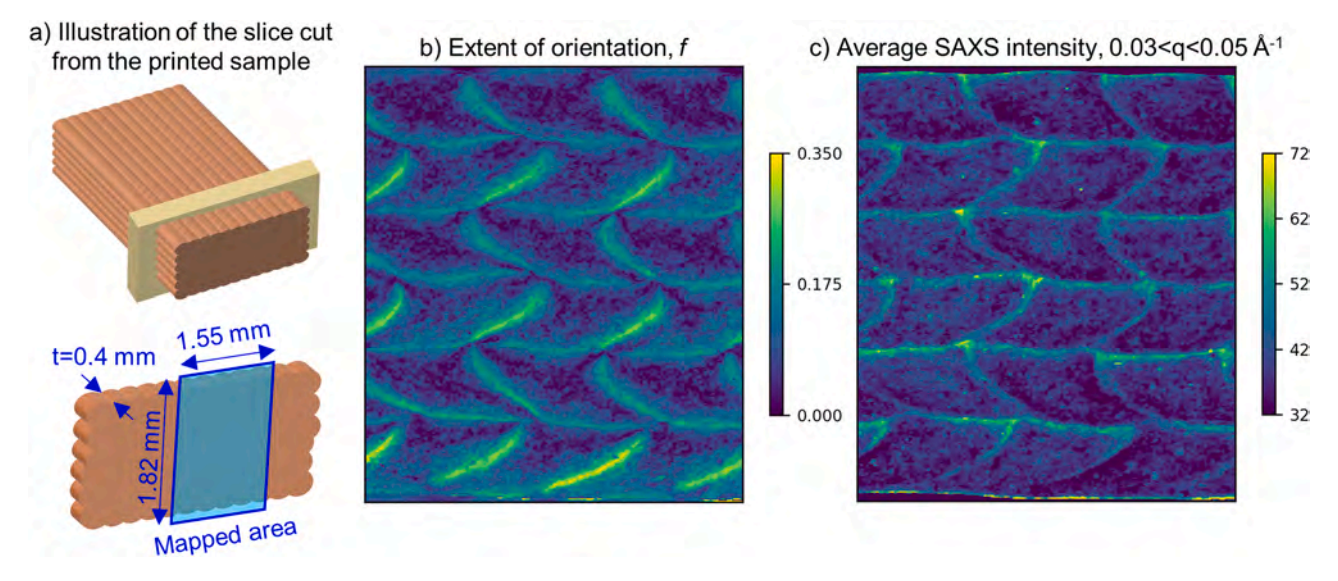


**Fig. 3.** (a) Illustration of the 0.4 mm-thick slice that was cut from the printed sample, orthogonal to the printing direction. (b) and (c) Images based on SAXS mapping of 3D-printed sample: (b) extent of orientation f, and (c) average SAXS intensity (arbitrary units) in the q range 0.03–0.05 Å<sup>-1</sup>. Each pixel corresponds to a SAXS pattern, and the images show a  $1.52 \times 1.74$  mm region of the sample. The top and bottom of the printed sample are visible; in (c), the regions of near-zero intensity at top and bottom are empty space (no sample).

# 2.8. SAXS comparison with optical microscopy

The 2D SAXS maps were compared with cross-polarized optical microscopy (POM) images by performing calculations based on a

phenomenological model. In POM, as a first-order simplification, when the polarization grating is oriented at  $0^{\circ}$  and the analyzer grating is oriented at  $90^{\circ}$ , some of the light passing through a sample oriented at  $45^{\circ}$  will pass through the analyzer. Meanwhile, a sample oriented at

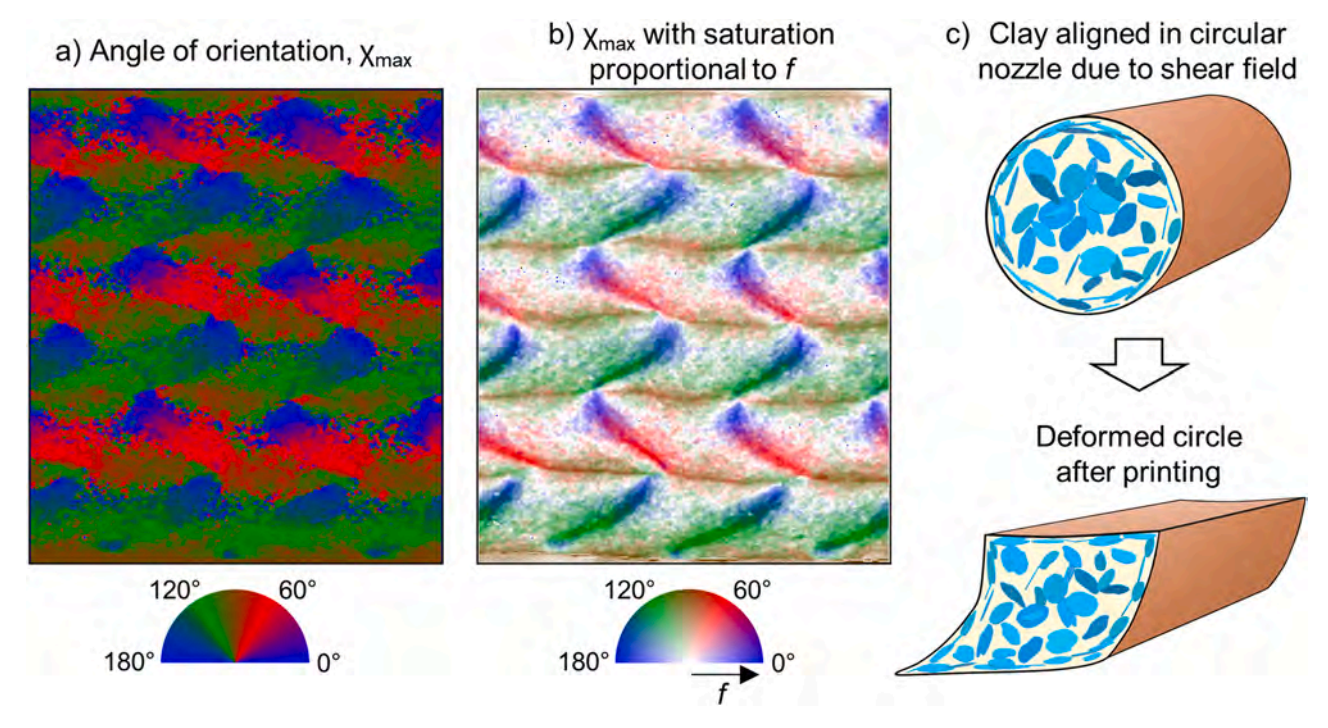


Fig. 4. (a) Angle of orientation,  $\chi_{max}$ , of each SAXS pattern, represented by a color as indicated by the angular color plot. (b) Same data as in (a), but the color saturation is proportional to the extent of orientation f (shown in Fig. 3b). White pixels indicate isotropic nanoclay orientation (f=0), while pixels with saturated colors correspond to regions with a high extent of orientation. (c) Schematic of clay alignment in the nozzle and after printing. The images shown in (a) and (b) are  $1.52 \times 1.74$  mm.

 $0^\circ$  or  $90^\circ$  will not alter the polarization of the incoming light and no light will pass through the analyzer. Thus, to convert from SAXS orientation to POM brightness, we use the function  $\sin^4(2\chi_{max})$ , which is peaked at  $\chi_{max}=45^\circ$ ,  $135^\circ$ , ..., and goes to zero at  $0^\circ$ ,  $90^\circ$ , ... Because the POM brightness should also increase with the extent of orientation f, we arrive at the following function:

$$B = f \sin^4(2\chi_{max}),\tag{6}$$

where *B* is the POM brightness of the irradiated region of the sample, as determined from the SAXS data. The good agreement between the POM image and *B* calculated from SAXS in Fig. 7 suggests that our simplifying assumptions are appropriate for this qualitative analysis.

# 3. Simulation of orientation dependent SAXS of platelets

The orientation of a platelet in space can be described by two Euler angles,  $\varphi$  and  $\psi$ . We define  $\varphi$  as the angle between the platelet normal vector and the incident X-ray beam, and  $\psi$  as the azimuthal rotation angle of the platelet normal vector, where the horizontal direction is  $0^\circ$  (see Fig. 2). With this definition, a platelet oriented co-planar with the substrate (Fig. 2b) would have  $\varphi=\psi=90^\circ$ . Separately,  $\chi$  is defined as the azimuthal angle on the detector, where the horizontal direction is  $0^\circ$ . Variations in  $\varphi$  and  $\psi$  give rise to different behavior in the 2D SAXS patterns, as shown in Fig. 2. According to these simulations of 2D SAXS, a platelet oriented face-on  $(\varphi=0^\circ)$  scatters weakly and isotropically in the detected region (Fig. 2a). Meanwhile, a platelet oriented edge-on  $(\varphi=90^\circ)$  scatters strongly along the direction of the platelet's normal vector (Fig. 2b). Thus, edge-on platelets show anisotropic intensity as a function of azimuthal angle (Fig. 2c), and also show significantly increased SAXS intensity when averaged over all  $\chi$  (Fig. 2d).

#### 4. Results and discussion

To investigate the morphology of the printed epoxy-based parts, cross-sections were cut orthogonal to the print direction (Fig. 3a). SAXS

and WAXS patterns were collected from every point on a square grid across the sample with 5  $\mu$ m spacing over an area of 2.8 mm². Each pattern was analyzed as discussed in the Methods section to extract several parameters, such as the extent of orientation, f (similar to the Hermans orientation parameter). Because the epoxy resin matrix is isotropic and homogeneous, the SAXS intensity is primarily due to the nanoclay. In these samples, the SAXS intensity follows a power law with respect to q ( $\Gamma$   $q^{-3}$ ), as shown in Fig. S1, consistent with a heterogeneous collection of plate like particles [31].

# 4.1. Neat epoxy-nanoclay sample

For the NC sample, Fig. 3b-c shows the extent of orientation, f, (see Eq. 3) and the overall intensity of each SAXS pattern in the 2D map. In each image, a tessellation of distorted parallelogram-like features is apparent. Fig. 3b shows that the extent of orientation is higher at the boundaries of the features, and near zero towards the middle of the features. This indicates that the nanoclay platelet azimuthal orientation is anisotropic at the feature borders and has nearly isotropic orientation away from those boundaries. Fig. 3c shows that the average SAXS intensity is higher at the boundaries. This is consistent with more of the nanoclay platelets being oriented edge-on, with their normal vectors orthogonal to the viewing plane ( $\phi$  biased towards  $90^{\circ}$ ) – see Fig. 2d. Away from the boundaries, the average SAXS intensity is lower, corresponding to random nanoclay orientation.

Several pieces of evidence indicate that the distorted parallelogram-like features correspond to individual printed roads. The average area of each feature is 0.148 mm², equivalent to a circle with diameter 0.43 mm. This is smaller than the nozzle diameter of 0.609 mm, but it corresponds closely to the expected area associated with each road, considering the 15% lateral overlap and 60% layer height that are programed into the g-code used to print the samples  $(0.85 \times 0.609 *0.6 *0.609 = 0.189 \text{ mm}^2)$ . Furthermore, it is well known that the highest shear rates occur near the walls of the nozzle during extrusion through the nozzle, and shear rates are low at the

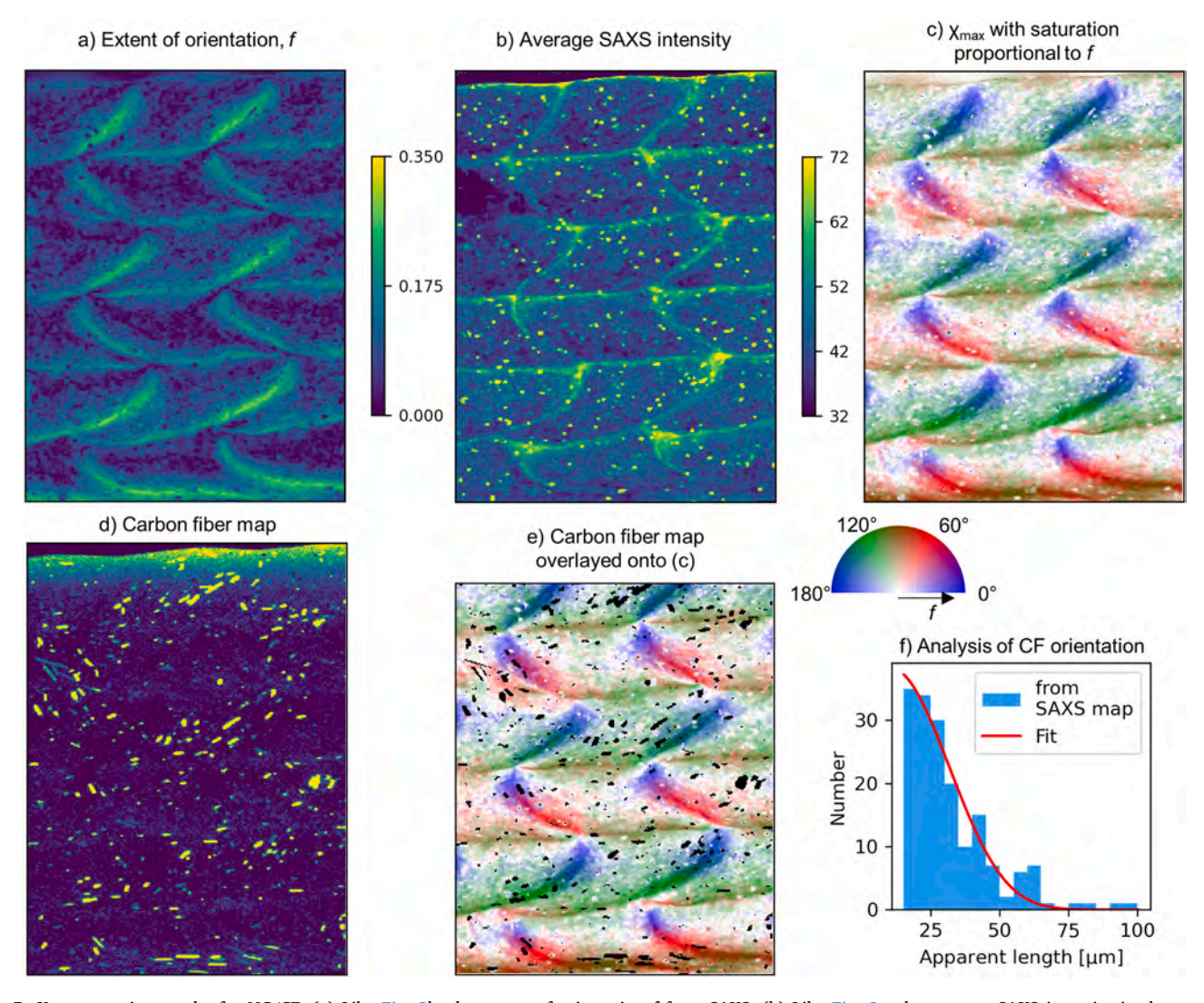


**Fig. 5.** X-ray mapping results for NC/CF. (a) Like Fig. 3b, the extent of orientation f from SAXS. (b) Like Fig. 3c, the average SAXS intensity in the q range 0.03–0.05 Å $^{-1}$  is shown. A bubble, causing lower intensity, is visible in the upper left corner. (c) Like Fig. 4b,  $\chi_{\text{max}}$  is indicated by the color, where the color saturation is proportional to f. (d) From WAXS, a map of the carbon fibers in the sample. (e) Carbon fiber map from (d), converted to a binary image and shown in black, overlaid onto the map shown in (c). (f) Histogram of the apparent lengths of the CFs from the binary CF map, and a fit to Eq. 5. The fit indicates that the standard deviation of the CF angle (relative to the printing direction) is 12.3°. (a)-(d) shows a 1.24 × 1.67 mm region of the sample, and (e) shows a 1.24 × 1.52 mm region.

center of the nozzle. Thus, it is logical that nanoclay platelets would have a high f at the edges of the nozzle and should be oriented edge-on along the print direction, while also parallel to the boundaries. This is consistent with the data in Fig. 3. The direct visualization of the road structure is remarkable in that it has not been observed before in the epoxy-nanoclay system using techniques such as SEM [1,10].  $\mu$ -SAX-S/WAXS is uniquely suited to perform this characterization.

This interpretation then enables determination of the order in which the roads were printed from Fig. 3c. The first road was printed in the bottom right corner of the image, with subsequent roads printed sequentially to the left. Then, the second layer was printed in the opposite order, beginning with the left-most road. This has been verified with the actual print path history of the sample. This also explains why the tilt direction of the parallelogram-like features alternate from layer to layer, forming a zigzagging pattern.

Fig. 4 shows the angle of orientation of the nanoclay throughout the sample. In Fig. 4a, the pixel color corresponds to the angle of orientation  $\chi_{max}$  of the scattering (which is normal to the nanoclay platelet plane), as indicated by the semicircular color bar. The angle of orientation clearly follows a systematic pattern, but interpretation of Fig. 4a is difficult without relating it to the road structure. Fig. 3b shows that the extent of

orientation is very low in much of the sample, and in those regions the angle of orientation has limited significance. Fig. 4b shows the same map as 4a, except that the color saturation of each point is proportional to its extent of orientation f (e.g., a white pixel indicates isotropic nanoclay orientation, where f=0). Now the road boundaries are visible, and this emphasizes that  $\chi_{max}$  is always normal to them near those boundaries. This further verifies that nanoclay platelets are predominantly oriented coplanar at and with the boundaries. This is consistent with previous in situ SAXS on a similar system during printing, where the nanoclay platelets at the top of the printed road were oriented parallel to the substrate [32].

Fig. 4c illustrates our hypothesis concerning the orientation of the nanoclay platelets in the nozzle and after printing. In the nozzle, the shear field is high near the walls, and this aligns the platelets such that they tend to be coplanar with nearby walls. When the extrudate is deposited, its cylindrical shape is deformed, but the platelets retain some of their orientation. This wall shear effect alone could explain the observations in the SAXS data, but there is another process that may have an equally, if not more, important effect: the shearing between a road being deposited and the previous road. To minimize voids, our printing program is set up such that when a road is printed, it pushes into the

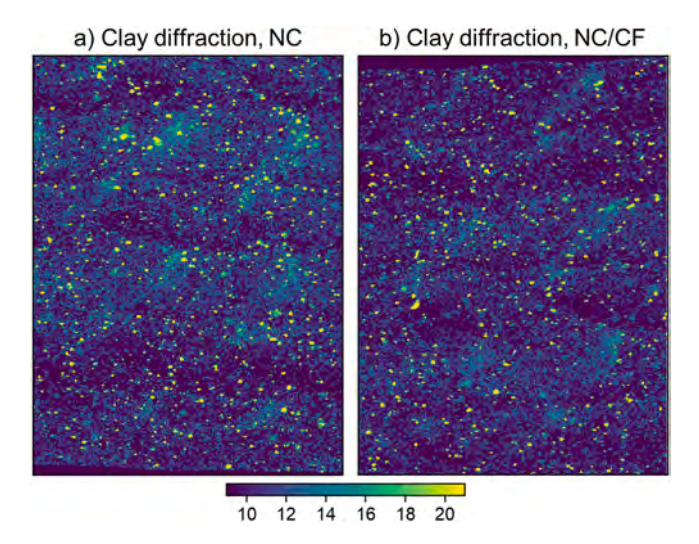
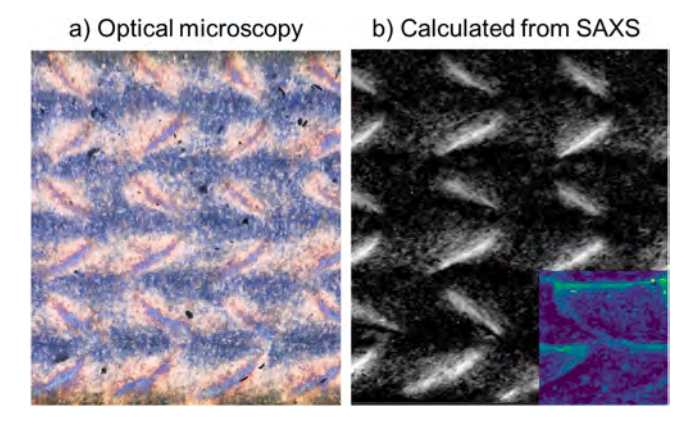


Fig. 6. Maps of clay diffraction intensity in WAXS for (a) NC sample, and (b) NC/CF sample shown at the same scale. The images show  $1.24\times1.67$  mm sample regions.



**Fig. 7.** Comparison of (a) experimental POM image with (b) calculation of microscope image from SAXS data using Eq. 6. In the lower right corner of (b), Fig. 3c is overlaid to highlight the relationship between the POM calculation and the scattering intensity. Both (a) and (b) show  $1.52 \times 1.74$  mm regions of the sample, but the precise locations on the sample are different.

previous road, significantly deforming it and causing shear. This likely explains why in Fig. 3b the diagonal road boundaries have higher extent of orientation than the horizontal road boundaries – when a road is printed, its lateral neighbor is much more deformed than its neighbor below. Further studies are needed to deconvolute the effects of in-nozzle shear and road-to-road shear on the morphology seen in the SAXS maps because it is further complicated by a 90° turn of the extrudate from nozzle to build platform [32].

# 4.2. Sample containing carbon fiber

A second sample was printed, termed NC/CF, containing carbon fiber (CF) at a concentration of 0.7 vol% to improve mechanical performance of printed coupons. Based on polarized optical microscopy images, the initial hypothesis was that the CFs influence the clay morphology. The same X-ray mapping procedure was performed on this sample. SAXS maps from the NC/CF sample are shown in Fig. 5a-c, mapping f, average SAXS intensity, and  $\chi_{max}$  as in Figs. 3b, c, and 4b. Interestingly, the SAXS maps do not show a qualitative difference in nanoclay orientation in the two samples; their nanoclay orientations relative to the road structures are practically identical. The presence of CF does not qualitatively change the nanoclay morphology. However, there are small features in

the NC/CF SAXS maps that are not present in the NC maps. These features are most clearly seen in Fig. 5b, as they scatter strongly at small angles. They are not due to streak scattering from the CFs (an example of which is shown in Fig. S2), as we will show below. Further studies are currently underway to determine micro void distribution and location via X-ray CT and microscopy techniques.

To map the carbon fibers, we analyze the WAXS pattern at each point, specifically using the intensity of the graphitic diffraction at  $q \approx 1.8 \, {\rm \AA}^{-1}$ . This mapping method is related to HAADF-STEM. The result is shown in Fig. 5d, where the carbon fibers are clearly visible. Note that the fiber positions do not overlap with or correspond to the high-SAXS intensity features in Fig. 5b as discussed above (also see Fig. S3). Some fibers appear as small circles because their axes are oriented into the page, while others are oriented at oblique angles and appear as short rods. In Fig. 5e, the carbon fibers are shown in black and superimposed onto the map shown in Fig. 5c. The carbon fiber concentration is not entirely uniform, with some roads containing more fibers than others. The fiber orientation appears to be influenced by the shear generated during printing. Many of the fibers at oblique angles appear to be aligned coplanar with the nearby nanoclay. For instance, at the bottom center of the image, the nanoclay is oriented coplanar with the substrate, and the fibers also lie in that plane (i.e., the projections of the fibers are horizontal).

The extent of orientation of the CFs can be estimated from their apparent lengths (as projected onto the mapping plane), because a CF that is perfectly aligned along the printing direction (into the page) will appear as a circle in the 2D projection. We use a conservative (low-end) estimate of 100  $\mu m$  for the average CF length. A histogram of the apparent lengths is shown in Fig. 5f, and is fit with Eq. 5, a function based on the assumption that the CF orientation distribution is Gaussian and is centered around the printing direction. The fit indicates that the standard deviation in the CF misalignment relative to the printing direction is  $12.3^{\circ}$ , which corresponds to a Hermans orientation parameter of 0.93.

The nanoclay itself can also be mapped via WAXS. The diffraction pattern of the nanoclay is complex (Fig. S4) and peaks could not be assigned unambiguously, due to varying intercalation states and overlapping peaks. As a result, mapping individual reflections is not informative. However, the intensity sum of the primary nanoclay diffraction peaks in the range  $1.3\text{--}2.5~\text{Å}^{-1}$  is mapped in Fig. 6 for both samples. Because the diffraction peak sharpness increases with particle size, this map essentially reveals the locations of clay tactoids or larger aggregates. These aggregates are about 5–10  $\mu m$  in diameter (spanning several pixels), are present in both samples at roughly equal concentrations, and are well dispersed. There may also be smaller aggregates present that are not easily detectable here.

# 4.3. Comparison with optical microscopy

As indicated above, we used POM to characterize these epoxynanoclay samples printed by DIW [10]. An intriguing pattern was observed, shown in Fig. 7a for the NC sample, although interpretation proved challenging without additional information. To aid in the understanding of this pattern, an approximate recreation of the optical image was calculated from the SAXS data using Eq. 6. Good qualitative agreement is observed in Fig. 7. Comparison with Figs. 3 and 4 shows that features visible in POM correspond to the diagonal boundaries of the roads. The horizontal road boundaries (top and bottom of each road) are not visible in Fig. 7b because the nanoclay orientation is horizontal (0°) here, parallel to the polarizing filter. We have confirmed that these horizontal boundaries become visible upon rotation of the sample in the microscope. Thus, with the inclusion of results from  $\mu\textsc{-}SAXS/WAXS$ , it is now possible to verify that road boundaries are directly visible in POM. This finding will enable researchers to map the road boundaries simply using optical microscopy, a widely accessible technique. It should be noted that beyond this road boundary mapping, POM provides very

limited morphological information compared with  $\mu$ -SAXS/WAXS. It is also obvious that POM will not work on samples with high CF loadings due to absorption of the light. Higher loadings can therefore only be traced with methods such as X-ray scattering that penetrate the entire sample and probe the micron and nanometer scales.

#### 5. Conclusion

We performed µ-SAXS/WAXS on 3D-printed samples, obtaining 225,060 scattering patterns over a sample area of 2.8 mm<sup>2</sup> for each sample. Each SAXS pattern was analyzed to obtain the extent of orientation f of the nanoclay, as well as the angle of orientation  $\chi_{max}$ . By creating images from the array of SAXS patterns, the printed road geometry was directly visualized (not seen before in printed epoxynanoclay materials) and key structural information was superimposed. The nanoclay platelets in the NC sample exhibited a high extent of orientation near the road boundaries, where the platelets were approximately coplanar with the road boundaries. Meanwhile, the nanoclay was mostly isotropic towards the centers of the roads. In the sample with reinforcing carbon fibers, the fibers were clearly visualized and identified by mapping the WAXS intensity from graphitic diffraction peak. The nanoclay morphology was qualitatively similar to the sample without carbon fibers, suggesting that the fibers had a negligible effect on the nanoclay morphology. Clay aggregates were visualized via WAXS in both samples. The aggregates are well-dispersed and have an approximate size of 5-10 µm. To compare with polarized optical microscopy, the SAXS data was used to simulate an optical microscopy image. The observed pattern was reproduced, demonstrating that optical microscopy directly reveals the diagonal road boundaries.

These results demonstrate that  $\mu$ -SAXS/WAXS is a powerful technique for probing nanoclay orientation and road structure in a printed part, coupon or article. A crucial next step is to use this tool to better understand the relationship between print parameters (e.g., speed, nozzle design) and mechanical properties [12]. For instance, shear-alignment of nanoclay can be enhanced with higher print speed or optimized nozzle surfaces and geometries. With the characterization tool demonstrated in this work, these effects can be quantified, and thereby the resulting mechanical properties can be understood down to the nanoscale level. Furthermore, given the interpretation of the microscopy provided in this work, the effect of print parameters on the road structure can be studied directly using the widely accessible technique of polarized optical microscopy, provided the inks are transparent enough for light transmission.

#### **Funding**

This research was performed while E.B.T. held an NRC Research Associateship award at the Air Force Research Laboratory (Wright-Patterson Air Force Base, Ohio). This project received funding from AFOSR under Dr. Jaimie Tiley and Ming-Jen Pan under the Low Density Portfolio #17RXCOR436. N.S.H and B.G.C would like to acknowledge funding from NSF under grant no. CMMI-1825815, and Honeywell Federal Manufacturing and Technologies through Contract DE-NA0002839, administrated by Dr. Jamie Messman, Mr. Steven Patterson, and Dr. Eric Eastwood. This work is based upon research conducted at the Materials Solutions Network at CHESS (MSN-C) which is supported by the Air Force Research Laboratory under award FA8650-19-2-5220.

# CRediT authorship contribution statement

**Edward Trigg:** Methodology, Software, Formal analysis, Writing – Original Draft, Writing – Review and Editing, Visualization. **Nadim Hmeidat:** Methodology, Validation, Investigation, Resources, Writing – Review and Editing. **Louisa Smieska:** Methodology, Software, Resources, Data curation, Writing – Review and Editing. **Arthur Woll:** 

Methodology, Software, Resources, Data curation, Writing – Review and Editing, Supervision. **Brett Compton:** Supervision, Funding acquisition, Resources, Writing – Review and Editing. **Hilmar Koerner:** Conceptualization, Supervision, Writing – Review and Editing, Project administration, Funding acquisition.

# **Declaration of Competing Interest**

The authors declare that they have no known competing financial interests or personal relationships that could have appeared to influence the work reported in this paper.

# Appendix A. Supporting information

Supplementary data associated with this article can be found in the online version at doi:10.1016/j.addma.2020.101729.

# References

- B.G. Compton, J.A. Lewis, 3D-printing of lightweight cellular composites, Adv. Mater. 26 (2014) 5930–5935, https://doi.org/10.1002/adma.201401804.
- [2] L.R. Holmes, J.C. Riddick, Research summary of an additive manufacturing technology for the fabrication of 3D composites with tailored internal structure, JOM 66 (2014) 270–274, https://doi.org/10.1007/s11837-013-0828-4.
- [3] C. Yang, X. Tian, D. Li, Y. Cao, F. Zhao, C. Shi, Influence of thermal processing conditions in 3D printing on the crystallinity and mechanical properties of PEEK material, J. Mater. Process. Technol. 248 (2017) 1–7, https://doi.org/10.1016/j. jmatprotec.2017.04.027.
- [4] A. Kotikian, R.L. Truby, J.W. Boley, T.J. White, J.A. Lewis, 3D printing of liquid crystal elastomeric actuators with spatially programed nematic order, Adv. Mater. 30 (2018) 1–6, https://doi.org/10.1002/adma.201706164.
- [5] S. Gantenbein, K. Masania, W. Woigk, J.P.W. Sesseg, T.A. Tervoort, A.R. Studart, Three-dimensional printing of hierarchical liquid-crystal-polymer structures, Nature 561 (2018) 226–230, https://doi.org/10.1038/s41586-018-0474-7.
- [6] X. Kuang, D.J. Roach, J. Wu, C.M. Hamel, Z. Ding, T. Wang, M.L. Dunn, H.J. Qi, Advances in 4D printing: materials and applications, Adv. Funct. Mater. 29 (2019) 1–23, https://doi.org/10.1002/adfm.201805290.
- [7] A.D. Cozier, K.E. Harned, M.A. Riley, B.H. Raabe, A.D. Sommers, H.A. Pierson, Additive manufacturing in the design of an engine air particle separator, in: Proc. ASME 2015 Int. Mech. Eng. Congr. Expo., 2015. https://doi.org/10.1115/ IMECE2015-51592.
- [8] J.P. Lewicki, J.N. Rodriguez, C. Zhu, M.A. Worsley, A.S. Wu, Y. Kanarska, J. D. Horn, E.B. Duoss, J.M. Ortega, W. Elmer, R. Hensleigh, R.A. Fellini, M.J. King, 3D-printing of meso-structurally ordered carbon fiber/polymer composites with unprecedented orthotropic physical properties, Sci. Rep. 7 (2017) 1–14, https://doi.org/10.1038/srep43401.
- [9] Y. Kanarska, E.B. Duoss, J.P. Lewicki, J.N. Rodriguez, A. Wu, Fiber motion in highly confined flows of carbon fiber and non-Newtonian polymer, J. Non-newton. Fluid Mech. 265 (2019) 41–52, https://doi.org/10.1016/j.jnnfm.2019.01.003.
- [10] N.S. Hmeidat, J.W. Kemp, B.G. Compton, High-strength epoxy nanocomposites for 3D printing, Compos. Sci. Technol. 160 (2018) 9–20, https://doi.org/10.1016/j. compscitech.2018.03.008.
- [11] H.A. Pierson, E. Celik, A. Abbott, H. De Jarnette, L. Sierra Gutierrez, K. Johnson, H. Koerner, J.W. Baur, Mechanical properties of printed epoxy-carbon fiber composites, Exp. Mech. 59 (2019) 843–857, https://doi.org/10.1007/s11340-019-00498-z.
- [12] N.S. Hmeidat, R.C. Pack, S.J. Talley, R.B. Moore, B.G. Compton, Mechanical anisotropy in polymer composites produced by material extrusion additive manufacturing, Additive Manufacturing 34 (2020) 101385.
- [13] B.G. Compton, N.S. Hmeidat, R.C. Pack, M.F. Heres, J.R. Sangoro, Electrical and mechanical properties of 3d-printed graphene-reinforced epoxy, JOM 70 (2018) 292–297, https://doi.org/10.1007/s11837-017-2707-x.
- [14] N. Nawafleh, E. Celik, Additive manufacturing of short fiber reinforced thermoset composites with unprecedented mechanical performance, Addit. Manuf. 33 (2020), 101109. https://doi.org/10.1016/j.addma.2020.101109.
- [15] Z.H. Sang, X.L. Xie, S.Y. Zhou, Y. Li, Z. Yan, L. Xu, G.J. Zhong, Z.M. Li, Gradient structure of crystalline morphology in injection-molded polylactide parts tuned by oscillation shear flow and its influence on thermomechanical performance, Ind. Eng. Chem. Res. 56 (2017) 6295–6306, https://doi.org/10.1021/acs.iecr.7b00930.
- [16] H. Zhang, A.K. Scholz, J. De Crevoisier, D. Berghezan, T. Narayanan, E.J. Kramer, C. Creton, Nanocavitation around a crack tip in a soft nanocomposite: a scanning microbean small angle X-ray scattering study, J. Polym. Sci. Part B Polym. Phys. 53 (2015) 422–429, https://doi.org/10.1002/polb.23651.
  [17] A. Gourrier, W. Wagermaier, M. Burghammer, D. Lammie, H.S. Gupta, P. Fratzl,
- [17] A. Gourrier, W. Wagermaier, M. Burghammer, D. Lammie, H.S. Gupta, P. Fratzl, C. Riekel, T.J. Wess, O. Paris, Scanning X-ray imaging with small-angle scattering contrast, J. Appl. Crystallogr. 40 (2007) 78–82, https://doi.org/10.1107/ S0021889807006693.
- [18] F. Schaff, M. Bech, P. Zaslansky, C. Jud, M. Liebi, M. Guizar-Sicairos, F. Pfeiffer, Six-dimensional real and reciprocal space small-angle X-ray scattering tomography, Nature 527 (2015) 353–356, https://doi.org/10.1038/nature16060.

- [19] A. Nohales, L. Solar, I. Porcar, C.I. Vallo, C.M. Gómez, Morphology, flexural, and thermal properties of sepiolite modified epoxy resins with different curing agents, Eur. Polym. J. 42 (2006) 3093–3101, https://doi.org/10.1016/j. eurpolymj.2006.07.018.
- [20] A. Zotti, A. Borriello, M. Ricciardi, V. Antonucci, M. Giordano, M. Zarrelli, Effects of sepiolite clay on degradation and fire behaviour of a bisphenol A-based epoxy, Compos. Part B Eng. 73 (2015) 139–148, https://doi.org/10.1016/j. compositesb.2014.12.019.
- [21] A.A. Azeez, K.Y. Rhee, S.J. Park, D. Hui, Epoxy clay nanocomposites processing, properties and applications: a review, Compos. Part B Eng. 45 (2013) 308–320, https://doi.org/10.1016/j.compositesb.2012.04.012.
- [22] T. Lan, T.J. Pinnavaia, Clay-reinforced epoxy nanocomposites, Chem. Mater. 6 (1994) 2216–2219, https://doi.org/10.1021/cm00048a006.
- [23] S. Stoupin, T. Krawczyk, Z. Liu, C. Franck, Selection of CVD diamond crystals for X-ray monochromator applications using X-ray diffraction imaging, Crystals 9 (2019) 396, https://doi.org/10.3390/cryst9080396.
- [24] P. Heiney, Datasqueeze: a software tool for powder and small-angle X-ray diffraction analysis, Comm. Powder Diffr. Newsl. 32 (2005) 9–11.
- [25] G. Ashiotis, A. Deschildre, Z. Nawaz, J.P. Wright, D. Karkoulis, F.E. Picca, J. Kieffer, The fast azimuthal integration Python library: PyFAI, J. Appl. Crystallogr. 48 (2015) 510–519, https://doi.org/10.1107/S1600576715004306.

- [26] W. Maier, A. Saupe, A simple molecular statistical theory of the nematic crystalline-liquid phase, IZ Nat. 14 (1959) 882–889.
- [27] C. Burger, B.S. Hsiao, B. Chu, Preferred orientation in polymer fiber scattering, Polym. Rev. 50 (2010) 91–111, https://doi.org/10.1080/15583720903503494.
- [28] I. Bihannic, C. Baravian, J.F.L. Duval, E. Paineau, F. Meneau, P. Levitz, J.P. De Silva, P. Davidson, L.J. Michot, Orientational order of colloidal disk-shaped particles under shear-flow conditions: a rheological-small-angle X-ray scattering study, J. Phys. Chem. B. 114 (2010) 16347–16355, https://doi.org/10.1021/in105714v
- [29] T. Dabat, F. Hubert, E. Paineau, P. Launois, C. Laforest, B. Grégoire, B. Dazas, E. Tertre, A. Delville, E. Ferrage, A general orientation distribution function for clay-rich media, Nat. Commun. 10 (2019) 1–9, https://doi.org/10.1038/s41467-019-13401-0
- [30] M.D. Abràmoff, P.J. Magalhães, S.J. Ram, Image processing with imageJ, Biophotonics Int. 11 (2004) 36–41, https://doi.org/10.1117/1.3589100.
- [31] D.W. Schaefer, R.S. Justice, H. Koerner, R. Vaia, C. Zhao, M. Yang, J. Vale, Large-scale morphology of dispersed layered silicates, in: Mater. Res. Soc. Symp. Proc., 2005: pp. 57–62. https://doi.org/10.1557/proc-840-q3.3.
- [32] K.J. Johnson, L. Wiegart, A.C. Abbott, E.B. Johnson, J.W. Baur, H. Koerner, In operando monitoring of dynamic recovery in 3D-printed thermoset nanocomposites by XPCS, Langmuir 35 (2019) 8758–8768, https://doi.org/10.1021/acs.langmuir.9b00766.